InterPore JOURNAL

Original Research

UNDERSTANDING FRACTURE APERTURE AND PERMEABILITY EVOLUTION DUE TO CARBONATE MINERALIZATION UTILIZING 3D PRINTING

Md Fahim Salek[1], Harrish Kumar Senthil Kumar[2], Abdullah Al Nahian[1], Samsul Mahmood[3], Bryan S. Beckingham[2], Kyle Schulze[3], Lauren E. Beckingham[1]

[1]Department of Civil and Environmental Engineering, Auburn University, Auburn, AL, USA; [2]Department of Chemical Engineering, Auburn University, Auburn, AL, USA; [3]Department of Mechanical Engineering, Auburn University, Auburn, AL, USA

Correspondence to:
Lauren E. Beckingham,
leb@auburn.edu

How to Cite:
Salek, M. F., Kumar Senthil Kumar, H., Al Nahian, A., Mahmood, S., Beckingham, B., Schulze, K., & Beckingham, L. (2025). Understanding Fracture Aperture and Permeability Evolution due to Carbonate Mineralization Utilizing 3D Printing. *InterPore Journal*, 2(4), IPJ011225-6.
https://doi.org/10.69631/dpd8ha46

RECEIVED: 28. Apr. 2025
ACCEPTED: 7 Sept. 2025
PUBLISHED: 1 Dec. 2025

ABSTRACT

Caprock formations are a crucial part of subsurface-engineered systems. Composed largely of shale, caprocks act as natural barriers that prevent the upward migration of fluids, thereby ensuring the containment of stored substances in subsurface formations. Fractures in these formations are potential leakage pathways for stored fluids. Mineral precipitation reactions in these fractures, particularly calcite, can significantly restrict the fluid permeability, reducing leakage potential. However, predictive capabilities of mineral precipitation in fractures and associated permeability evolution are limited due to a lack of fundamental understanding of such reactions in natural samples, complicated by mineral heterogeneity and the complexity of the fracture structure. In this study, 3D-printed fracture samples are used to understand the impact of carbonate mineralization on fracture aperture and permeability evolution. Samples were printed using a digital light processing (DLP) 3D printer and commercial liquid resin. Calcite precipitation was first tested on printed 2D films before conducting plug flow column experiments aimed to understand fracture permeability changes due to mineral precipitation. Contact angle measurement and Fourier transform infrared (FTIR) spectroscopy on printed 2D films show evidence of a substantial amount of surface energy for calcite nucleation and precipitation. Surface topography analysis of printed fractured surfaces reveals comparable values, highlighting the high replicability of the printed samples. During the column experiments, the permeability reduces exponentially due to a decrease in fracture aperture. Reductions in fracture aperture estimated from effluent concentration and 3D X-ray computed tomography (CT) show comparable results. Moreover, 3D X-ray CT images suggest the impact of local flow velocities on precipitation. The insights gained from this research contribute to a deeper understanding of the permeability evolution due to carbonate mineralization in caprock formations.

KEYWORDS
3D printing, Rock fracture, X-ray computed tomography, Carbonate mineralization, Permeability evolution

1. INTRODUCTION

Caprock formations serve as natural barriers that inhibit the vertical movement of fluids through subsurface layers. Their low permeability prevents fluids such as hydrocarbons, groundwater, or injected substances (e.g., CO_2 for carbon storage) from migrating upward (3, 15, 19). Caprocks may contain induced or naturally occurring fractures, which can vary in size and connectivity, potentially influencing their overall permeability. Supersaturation of ions in formation brine, resulting from changes in pH, temperature, dissolved CO_2 levels, or dissolution of primary minerals, for example, can result in mineral precipitation (16). Such reactions in fractures can contribute to narrowing fracture aperture and reducing the available pathways for fluid flow, resulting in a significant decrease in fracture permeability (8, 30, 48).

Mineral nucleation and growth of crystals on the solid-water interface is critical for many environmentally engineered systems (11, 12). In geologic CO_2 sequestration systems, mineralization in fractures may be beneficial. By reducing fracture permeability, the containment of stored substances within underground reservoirs may be better maintained, improving the integrity and safety of subsurface storage systems (6, 7). However, this same reduction in permeability may pose challenges to enhanced geothermal and oil/gas extraction systems (18, 54). Understanding these processes at a detailed level is thus essential for predicting the long-term behavior and stability of subsurface systems.

Traditional laboratory experiments aimed at studying geochemical reactions in fractures are challenging due to the inherent heterogeneity and ultra-low permeability of natural samples (42, 45). Variability in mineral composition and structural differences within samples, even those from the same location, further complicate these studies, often leading to inconsistent results (4, 44). To address these limitations, researchers have employed simplified experimental setups, such as manually cutting rock samples to represent fractures. However, these methods fail to accurately replicate the natural fracture geometries and surface roughness (21).

Advancements in 3D printing technology have opened new avenues for creating highly controlled and replicable experimental models (2, 20, 36, 41, 46). Leveraging 3D printing, it is possible to produce detailed fractured matrices that closely mimic the physical characteristics of natural rock fractures (22, 31). Samples can then be used to understand the permeability and sealing capacity of caprock fractures due to mineral precipitation. This approach allows for precise control over experimental variables and enhances the reproducibility of results, providing a robust platform for investigating precipitation mechanisms and kinetics.

The majority of studies related to 3D printed fractures are about understanding the fluid flow characteristics through fractures, mechanical behavior under stress, and the effect of the material property on permeability (25, 37, 38, 52). Very limited research has been conducted to study carbonate mineralization in fractures utilizing this unique approach. Stoner et al. utilized stereolithography 3D printing to fabricate a synthetic fracture surface integrated into a micro-model to understand the microbial-induced calcite precipitation and its effect on the flow paths (51). Dilsiz and Mihcakan used the fused deposition method (FDM) to print a simple, artificial fracture model to investigate the behavior of precipitation in different temperatures, flow conditions, and fracture roughness, considering only bulk precipitation (13). Kumar et al. fabricated high impact polystyrene (HIPS) films using fused filament fabrication (FFF) and later used a surface functionalization technique to increase surface energies to promote controlled heterogeneous calcite precipitation on the film's surface. They extended this

approach to 3D printed HIPS porous media structures and observed calcite precipitation to fabricate replicates of reactive porous media structures (23).

This study will be the first to leverage 3D printing to enhance understanding of mineral precipitation in fractures at the pore scale and the impact of reactions on the evolution of fracture permeability. Here, realistic fracture models of naturally fractured rock samples are fabricated via digital light processing (DLP) 3D printing and used for examining the effect of calcite precipitation on fracture aperture and permeability evolution. A calcite supersaturated solution is injected into the printed cores to simulate the natural geochemical environment and observe the resulting calcite deposition patterns and its effects, leveraging 3D X-ray CT imaging to track changes at the pore scale.

The insights gained from this research will contribute to a deeper understanding of carbonate mineralization in rock fractures, offering enhanced predictive capabilities for subsurface engineering projects. This work also demonstrates the potential of integrating additive manufacturing technologies with traditional geochemical experimentation to overcome the limitations of natural sample variability and improve the accuracy of laboratory studies.

2. MATERIALS AND METHODS

2.1. Calcite Growth on 2D Film

To establish a benchmark for the column experiment, a calcite growth experiment was first conducted on 2D films at room temperature (22° Celsius) and atmospheric pressure. Two-dimensional films measuring 25 mm × 30 mm and 2 mm in thickness were 3D printed using a DLP printer[a] at a resolution of 0.050 mm with a tough resin[b]. The precipitation experiments were performed by mixing equal amounts of freshly prepared stock solution of sodium carbonate (0.005 M) and calcium chloride dihydrate (0.005 M) in a beaker. This mixed stock solution was then flowed through the 2D film holder, and the effluent was collected at the end of the film (**Figure S1**; available online with the **Supplementary Material**). The associated calcite saturation index of the solution was 1.87 (estimated using PHREEQC[c]). Lab-grade sodium carbonate and calcium chloride dihydrate were purchased from VWR BDH chemicals. A peristaltic pump[d] was used to maintain a flow rate of 1 ml/min over the DLP-fabricated 2D films. Four separate experiments were conducted for time periods of 1 hour, 4 hours, 8 hours, and 24 hours.

The weight of each DLP fabricated film was measured before and after the calcite precipitation experiment and compared to discern the weight of precipitated calcite. Before weighing, the reacted films were rinsed with deionized (DI) water and patted dry to remove residual solution. Scanning electron microscopy[e] (SEM) images were collected. Moreover, Fourier transform infrared (FTIR) spectroscopy was performed on the uncured resin, and the DLP fabricated 2D films using an FTIR instrument[f] equipped with attenuated total reflection (ATR). An optical tensiometer[g] was used to perform sessile drop contact angle measurement on the DLP fabricated 2D surfaces. Following the sessile drop method, the contact angle was determined at room temperature (22° Celsius) using 4µL DI water using a micro-pipette.

---

[a] *Anycubic M3 Max DLP Printer: https://store.anycubic.com/products/photon-m3-max*

[b] *Anycubic Touch Resin: https://store.anycubic.com/products/uv-tough-resin?_sasdk=dMTlhMjcwMzA5ZTc0OWYtMDFlMWNjYmFkMWZmNGM0LTg1MTUwMjQtMjM1OTI5Ni0xOWEyNzAzMDllOGUyNA&utm_campaign=how_to_choose_the_right_resin_for_3d_printing_202301&utm_medium=guides&utm_source=blog*

[c] *PHREEQC Version 3: https://www.usgs.gov/software/phreeqc-version-3*

[d] *INTLLAB BT100: https://www.amazon.com/INTLLAB-Variable-Peristaltic-0-06-360-0-1-100rpm/dp/B082K97W5W*

[e] *Zeiss Evo 10: https://www.zeiss.com/microscopy/en/products/sem-fib-sem/sem/evo.html*

[f] *Thermo Scientific Nicolet 6700 FT-IR instrument: https://www.americanpharmaceuticalreview.com/25304-Pharmaceutical-Infrared-Spectroscopy-Equipment-Infrared-Spectrometers/5822268-Nicolet-6700-FT-IR-Spectrometer/*

[g] *Biolin Scientific Attension Theta Lite analyzer: https://www.biolinscientific.com/attension/optical-tensiometers/theta-lite*

Contact angle measurements were performed over three samples and averaged to obtain the mean contact angle.

2.2. Calcite Precipitation in Fracture Experiment

2.2.1. 3D Printing of Rock Fracture

A 3D X-ray micro-computed tomography (micro-CT) image of a fractured granite sample, downloaded from the Digital Porous Media Portal[h], was selected as the basis for 3D printing (56). The images had a voxel size of 54 microns. The downloaded data was processed to remove noise and microcracks using ImageJ[i] (43), keeping only a single major fracture in the model. The fracture was isolated from the solid structure based on variations in grayscale intensity. The identified region of interest (the solid) was then converted into a 3D mesh using Dragonfly[j]. Finally, the mesh was exported as a stereolithography (.stl) file and three replicate samples printed to original size using the DLP Printer[a] at 0.050 mm resolution using the tough resin[b]. The printed samples had a size of 1 inch in diameter and 1 inch long.

2.2.2. Fracture Surface Characterization

The surface topography of the three printed samples was analyzed to compare between samples. The surface profile was analyzed using a scanning white light interferometer[k] (SWLI). To ensure consistency and avoid uncertainties, measurements were taken from approximately the same location in a set orientation for all samples. A 1 mm x 1 mm scan was performed using the 5X objective at 1.0X magnification. The lateral resolution was 1.968 µm/pixel, and the vertical resolution was 100 nm. A forward scan of 500 µm and a back scan of 150 µm were utilized to capture all the height deviation in the region of interest. Raw data was then subjected to a tilt correction process by fitting it to a plane. Details of roughness parameter calculations are explained in the supporting information.

2.2.3. Column Experiment

Samples were prepared for the column flow-through experiment by wrapping in heat shrink tubing before installing inside a custom 3D-printed core holder in the flow-through experimental set-up (**Figure S2**; available online with the **Supplementary Material**). A dual-channel syringe pump[l] was used to inject $CaCl_2$ and $NaCO_3$ solution separately at a flow rate of 0.1 ml/min from each channel. Injection channels meet using a T-connector, resulting in a combined flow rate of 0.2 ml/min which was set to ensure laminar flow through the fracture. The solution concentrations and the saturation index were the same as in the 2D film experiments. Two experiments were conducted at room temperature (22° Celsius) for 12 hours (12H) and 16 hours (16H), respectively. A third experiment injecting DI water through the sample was carried out for 24 hours as a control experiment.

The transport condition can be characterized by the dimensionless Peclet number (Pe), which represents the ratio between advective and diffusive time scales (**Eq. 1**).

$$Pe = \frac{ul}{D} \tag{1}$$

where u is the average velocity through the fracture (m/s), l is the characteristic length (m), and D is the diffusion coefficient of Ca^{2+}, where a value of 1.4×10^{-9} m^2/s at 25° C was used (49). The average velocity was calculated from the flow rate; $u = Q/A$, where Q is the volumetric flow rate (m^3/s) and A is the average area of the fracture opening (m^2).

[h] *https://digitalporousmedia.org/digital-rocks-portal-tombstone/*
[i] *https://imagej.net/ij/*
[j] *https://dragonfly.comet.tech/*
[k] *Bruker Contour GTK Scanning White Light Interferometry: https://www.bruker.com/de/products-and-solutions/test-and-measurement/3d-optical-profilers.html*
[l] *Chemyx: https://chemyx.com/syringe-pumps/fusion-200x/*

The relative rate of reaction (R) in comparison to advective transport is reflected in the dimensionless Damköhler number (Da), defined as follows from Lasaga (24; **Eq. 2**):

$$Da = \frac{Rl}{u} \tag{2}$$

For precipitation, we interpret reaction time to be the time taken to precipitate over the characteristic length l. As we are considering a core scale reaction, the characteristic length is the length of the core sample L. Nilsson and Strenbeck reported the reaction rate constant for calcite precipitation in a supersaturated batch experiment as $k_{calcite} = 3.81x10^{-7}\ mol/m^2s$ (34). For the fracture surface, the reaction rate can be determined from $R = k_{calcite} * a$ (58), where a is the fracture surface area. The surface area here is determined from the SWLI experiment.

2.2.4. Effluent Analysis and Pressure Measurement

Effluent samples were collected in 50 ml test tubes at set time intervals for both experiments. The samples were acidified and then analyzed for Ca and Na concentrations using an ion chromatograph[m]. The Ca ion concentrations were used to calculate the total volume of calcite precipitation and aperture reduction ($T_{precipitation}$), assuming a flat surface and homogenous precipitation, as given by (**Eq. 3**):

$$T_{precipitation} = \frac{\sum(C_{in,i} - C_{out,i})\ M_{calcite}\ t_i\ Q}{M_{Ca^+}\ \rho_{calcite}\ L\ D} \tag{3}$$

Here, C_{in} and C_{out} are the influent and effluent concentrations of Ca^+ (g/m^3), $M_{calcite}$ and M_{Ca^+} are the molar mass of calcite and Ca^+ (g/mol), t_i is the time interval (s), and $\rho_{calcite}$is the density of calcite (2.71 g/cm^3). Caulk et al. (9) used a similar approach to calculate the fracture aperture change due to mineral dissolution in fractured granite.

A pressure transducer measured the pressure difference between the inlet and outlet throughout the experiment. The pressure measurements were used to estimate the fracture permeability using Darcy's law (**Eq. 4**):

$$Q = \frac{kA\Delta P}{\mu L} \tag{4}$$

where Q is the volumetric flow rate (m^3/s), k is the permeability of the specimen (Darcy), ΔP is the pressure difference between upstream and downstream (Pa), μ is the dynamic viscosity (Pa.s), and L is the length of the sample (m). Using the pressure measurement, the fracture aperture was estimated using the cubic law (57; **Eq. 5**).

$$Q = \frac{\Delta P b^3 d}{12\mu L} \tag{5}$$

Here, b is the fracture aperture (m), d is the aperture width, and L is the length of the specimen (m).

2.2.5. 3D X-ray Imaging and Image Processing

X-ray micro-computed tomography (micro-CT) scans were carried out on the intact sample while mounted inside the printed core holder using a micro-CT scanner[n] with a resolution of 30 microns. Before imaging, the samples were flushed with DI water and air dried at room temperature. As the field of view of the X-ray instrument is shorter than the sample height, sample collection consisted of three

[m] *Thermoscientific Dionex Aquion Ion Chromatographer: https://lis.turklab.info/Upload/Product/en/dionex-aquion-system/ebc2e22e84c939894db780612edd30c4.pdf*

[n]Zeiss Xradia Versa 620 Scanner: *https://nanousers.mit.edu/characterizenano/focus-facilities/xray-diffraction/zeiss-xradia-versa-620-micro-ct*

vertical scans stitched together during reconstruction. The raw data were reconstructed using the instrument's built-in reconstruction software[o].

A non-local means (NLM) filter was applied using ImageJ to improve the image quality of the collected image stack. As the calcite and the printed material have different X-ray attenuations, these phases can be differentiated based on grayscale intensity in the 3D image. For analysis, the fracture area was cropped and then thresholded to isolate low, high, and intermediate-intensity voxels that correspond to the voids, calcite, and printed polymer, respectively. The average reduction in fracture aperture (T_{image}) was calculated assuming a flat surface as (**Eq. 6**):

$$T_{image} = \frac{Number\ of\ Calcite\ Pixels\ X\ Image\ Voxel\ Size^3}{L\ X\ D} \quad (6)$$

Here, L and D are the length and diameter of the sample (m), respectively.

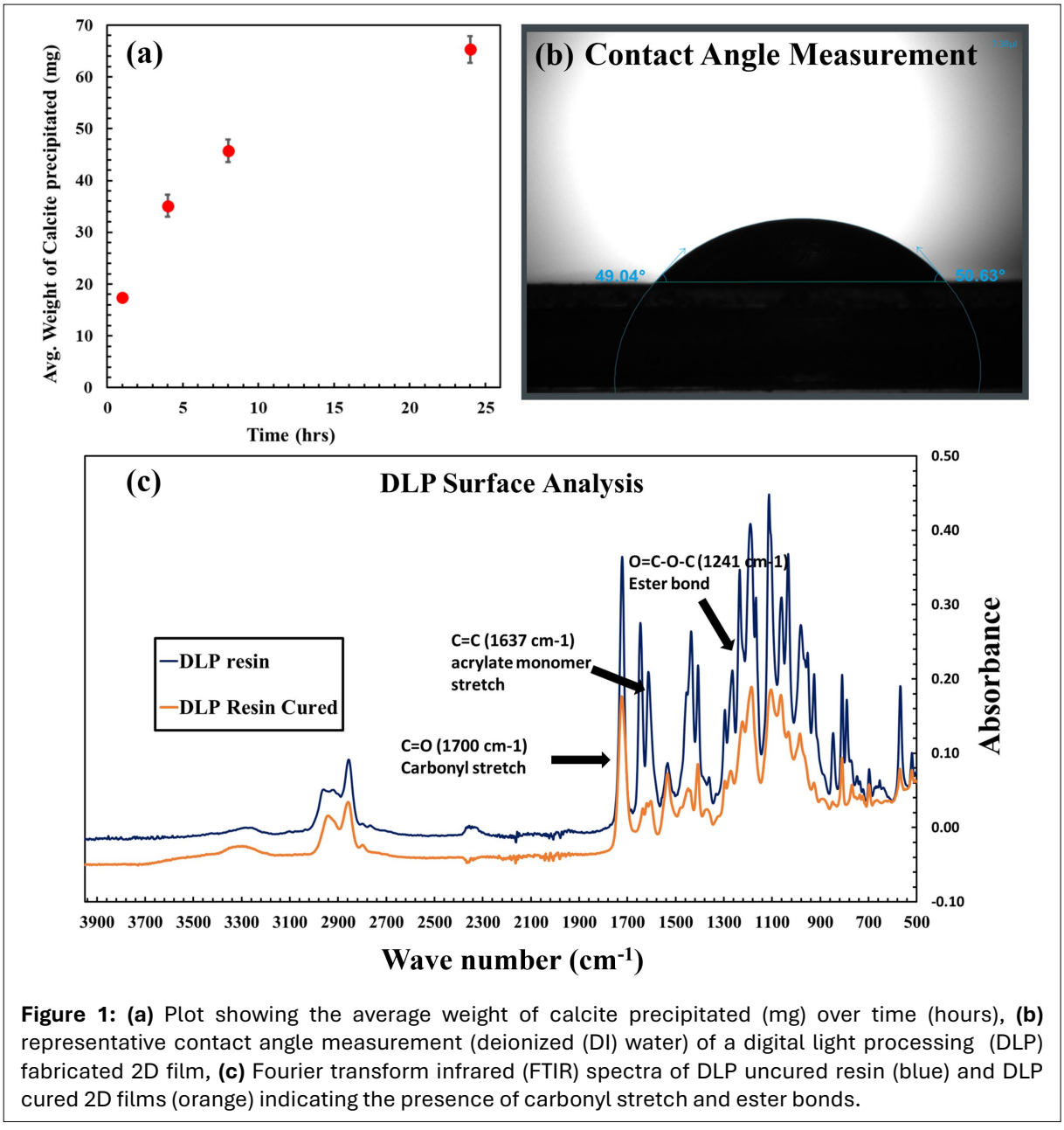

Figure 1: (a) Plot showing the average weight of calcite precipitated (mg) over time (hours), **(b)** representative contact angle measurement (deionized (DI) water) of a digital light processing (DLP) fabricated 2D film, **(c)** Fourier transform infrared (FTIR) spectra of DLP uncured resin (blue) and DLP cured 2D films (orange) indicating the presence of carbonyl stretch and ester bonds.

[o] Zeiss Scout and Scan Control System Reconstructor: *https://www.zeiss.com/microscopy/us/l/campaigns/scout-and-scan.html*

2.2.6. Scanning Electron Microscopy Analysis

High-resolution secondary electron (SE) and energy-dispersive spectroscopy (EDS) images were collected from the fracture surface using a scanning electron microscope (SEM)[p]. Images were used to characterize texture and to identify calcium. The printed material is nonconductive to electricity, so the surface was coated with gold using a sputter coater before imaging.

3. RESULTS

3.1. Calcite Growth on 2D Film

The amount of calcite precipitating on the 2D film increases logarithmically with time (**Fig. 1a**). SEM images of the reacted 2D films show an increase in the amount of precipitated calcite over time (**Fig. S3**; available online with the **Supplementary Material**). Images also reveal uniform precipitation of calcite across the surface (**Fig. S3b**; available online with the **Supplementary Material**), suggesting the uniform properties of the surface. From the contact angle experiment, an average contact angle of 49.83° (**Fig. 1b**) is observed on the surface of the 2D films, indicating a moderate surface energy associated with these films, which helps calcite to overcome the surface energy barrier to precipitate (23). Fourier transform infrared spectroscopy of the uncured DLP resin and the DLP fabricated film (**Fig. 1c**) shows the presence of carbonyl and ester groups on the surface. Polar carbonyl and ester groups increase the surface energy, and hence decrease the contact angle, promoting favorable conditions for precipitation (10).

3.2. Fracture Surface Characteristics and Printing Replicability

Data obtained from the SWLI analyses were processed and analyzed to generate a surface topography map and calculate roughness parameters. **Figure 2a** shows the 3D surface topography taken from samples 1, 2 & 3, and **Figures 2b** and **2c** show the horizontal profiles across the X and Y axes, taken from the centerline of each map. Surface topography maps (**Fig. 2a**) of the three core samples suggest similar trends with occasional roughness variation of 40-50 µm, which is mostly due to the angular misalignment and randomness of the fracture surface. The horizontal profile plots across the centerline X and Y axes (**Fig. 2b-c**) also show comparable results between the samples.

Table 1: Surface roughness parameters of fracture surfaces

Sample name	S_a (µm)	S_{sk}	S_{ku}	S_{dr} (%)
Sample 1	32.83	0.025	2.355	49.25
Sample 2	31.28	0.159	2.562	56.98
Sample 3	32.2	0.003	2.597	45.64

The calculated surface roughness parameters (**Table 1**) for all three cores do not show significant variation in roughness across the three samples. There is good agreement in the S_a values, and the skewness values for all samples are positive and relatively small, indicating surfaces with slight asymmetry. The kurtosis values are also similar across the samples, where a value less than three indicates that the height distribution has lighter tails than the normal distribution. The comparable values of the developed interfacial area ratio (S_{dr}) also indicate that the captured topographies are similar. The slight variation observed in values for these parameters across different samples is likely because the analysis was conducted at slightly different locations on each sample.

3.3. Effluent Chemistry, Fracture Aperture Evolution (X-ray CT), and Permeability Evolution

Peclet and Damköhler numbers help understand the interplay between fluid flow, mass transport, and reaction kinetics. The calculated Pe number is 9×10^3. A very high Pe number represents an advection-

[p] *Zeiss Evo 10 SEM: https://www.zeiss.com/microscopy/us/l/campaigns/automate-and-correlate.html*

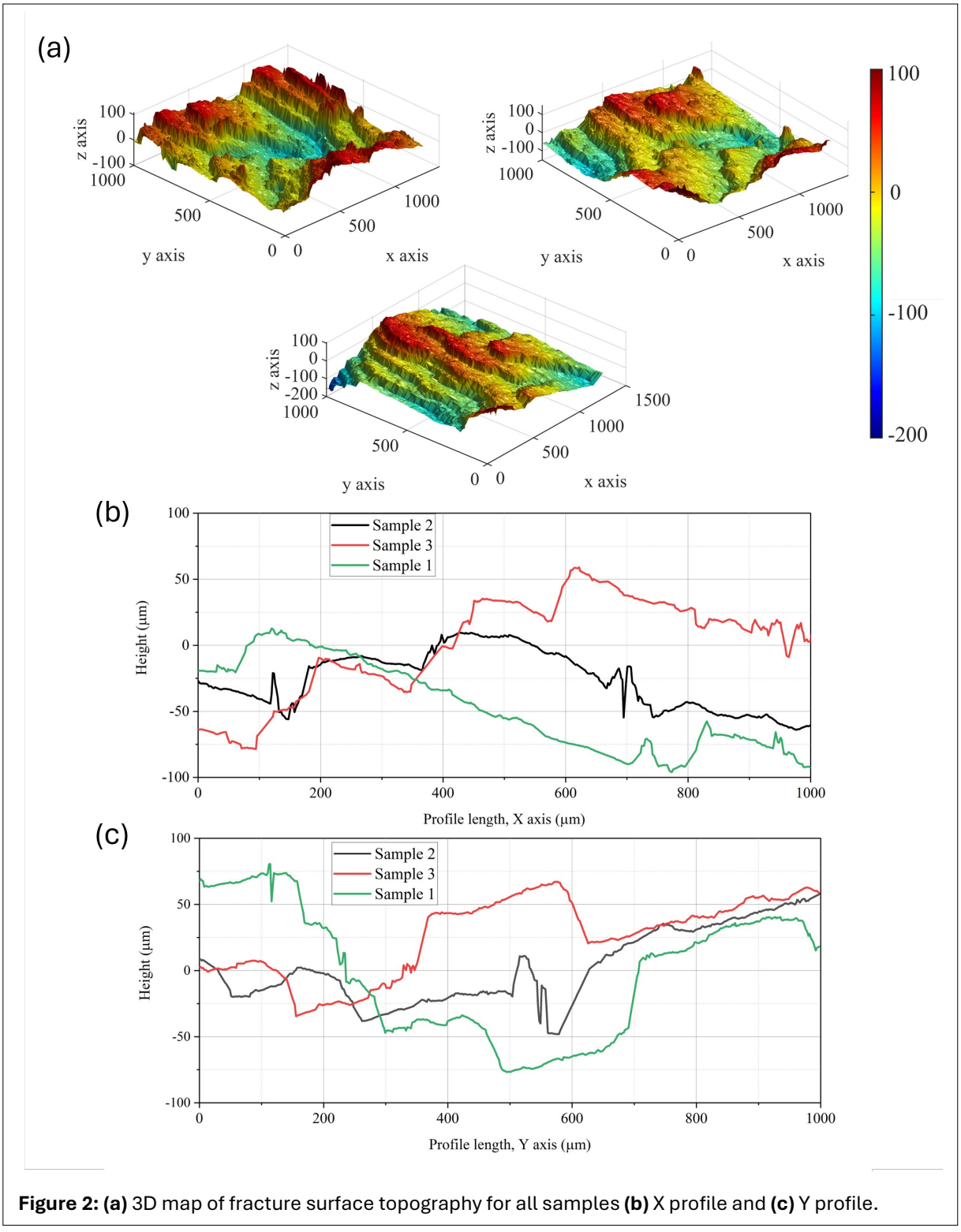

Figure 2: (a) 3D map of fracture surface topography for all samples **(b)** X profile and **(c)** Y profile.

dominant system. On the other hand, our estimated Damköhler number is 3.6 x 10^{-8}, which indicates that the reaction is significantly slower than the advection. These conditions are anticipated to correspond to uniform precipitation, as long as the surface characteristics are the same (53). However, the sample has variable roughness and variations in aperture, resulting in some local preference for precipitation as observed in **Figure 3**.

Samples collected from the effluent were analyzed using ion chromatography, and the data is shown in **Table 2**. The concentration of calcium in the effluent, is considerably less than the concentration in the stock solution (estimated 200 mg/L), supporting the assumption of calcite precipitation. Based on a mass balance of the effluent calcium concentrations, the estimated amounts of calcite precipitated are 32.12

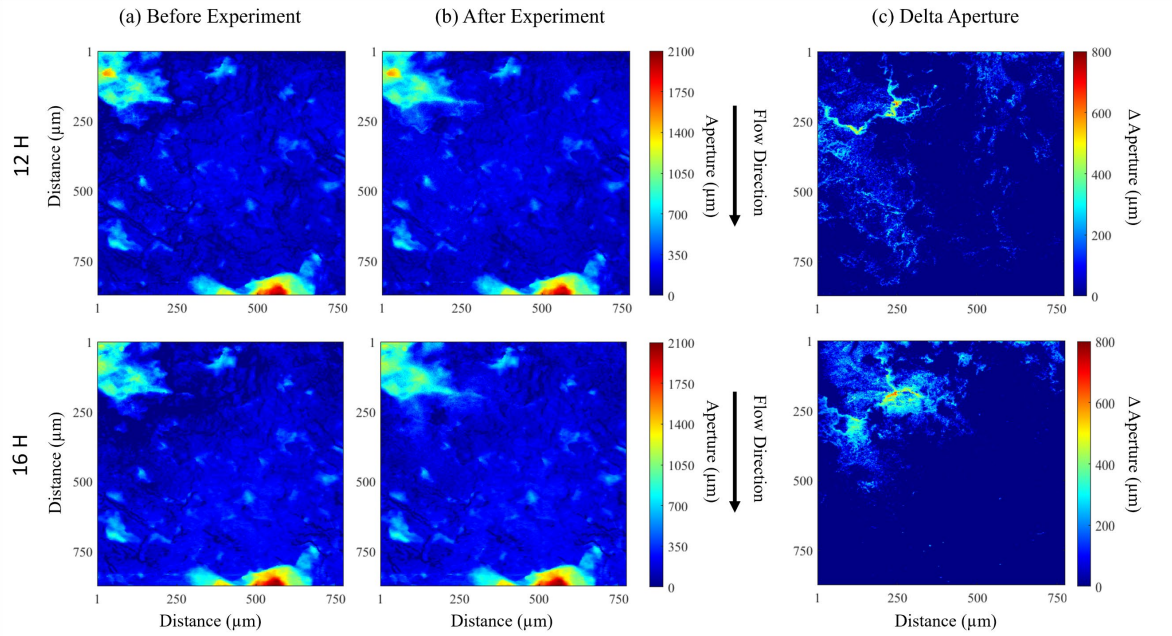

Figure 3: Fracture aperture evolution due to mineral precipitation as determined from processing 3D X-ray micro-CT images. The solution flow is top to bottom.

mg and 42.25 mg for the experiments with durations of 12 h and 16 h, respectively. The associated theoretical aperture reductions calculated using **Equation 3** are 22.45 µm and 29.47 µm (**Table 3**). A slight difference is observed in the sodium concentration in the effluent from the stock solution (estimated 114.95 mg/L), suggesting some NaCl precipitation on the fracture surface, which is also evident in the SEM images.

Three-dimensional X-ray micro-CT images show changes in fracture aperture due to calcite precipitation. Although the lower resolution (compared to the calcite particles) may impact the processed results, the overall goal was to characterize larger-scale fracture aperture reduction due to precipitation while fitting the whole sample within the instrument's field of view. The pre- and post-experiment images show considerable aperture reduction in some specific zones in both experiments (**Fig. 3**). The average reductions are calculated to be 30.52 µm and 25.61 µm, respectively, for experiments 12H and 16H (**Table 3**).

Processed aperture maps from 3D X-ray CT images (**Fig. 3a,b**) depict the spatial distribution of the fracture aperture before and after the experiment. The difference map (**Fig. 3c**) reflects the amount of

Table 2: Ion chromatography analysis results

Element	Effluent Concentration (mg/L)						
	Experiment 12H			Experiment 16H			
Duration	4 H	8 H	12 H	4 H	8 H	12 H	16 H
Ca	24.38	20.12	20.72	28.52	25.39	20.42	22.18
Na	109.89	107.98	114.94	108.53	109.73	110.87	105.97

Table 3: Estimated change in fracture aperture

Method	Reduction in Avg. Fracture Aperture (µm)	
	Experiment 12H	Experiment 16H
From effluent concentration (mass balance)	22.45	29.47
From 3D X-ray CT image (parallel plate theory)	25.61	30.52
From pressure measurements (cubic law)	43.98	44.19

 https://doi.org/10.69631/dpd8ha46

calcite precipitation in the fracture in terms of changing the fracture aperture. Similar precipitation patterns are evident in both experiments. However, the calcite precipitation pattern seems heterogeneous, with more precipitation occurring in the top-left corner near the inlet, where the aperture abruptly narrows down. Moreover, preferential precipitation on the left side of the sample indicates a preferential flow path starting from the broader aperture near the inlet on that side (35).

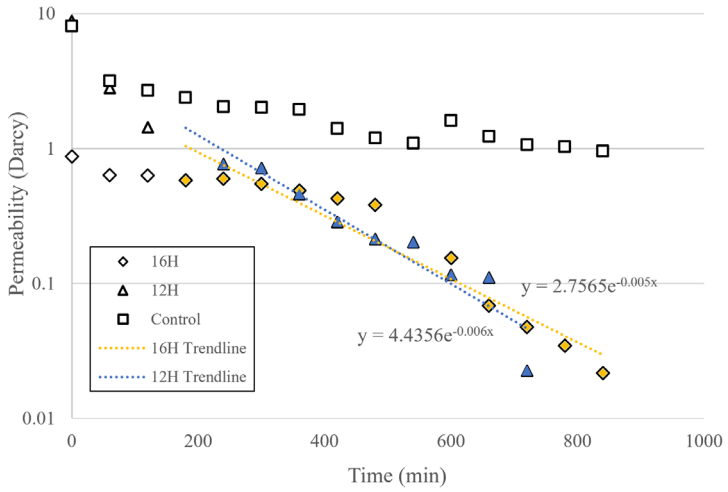

Figure 5: Experimental permeability evolution calculated from the differential pressure measurements. Data used for the trendlines are presented using colored markers: blue for the 12H experiment and yellow for the 16H experiment.

The estimated experimental permeability evolution determined from pressure measurements (**Fig. 4**) shows a reduction in permeability over time. The data for the 180 min (12H experiment) and 540 min (16H experiment) are not shown due to instability in the results caused by the syringe refilling step. The observed decreasing trend in permeability results from an increase in differential pressure from calcite precipitation. Between 240 and 660 minutes, both experiments exhibit a similar downward trend; however, the 12H experiment shows a sudden drop after 660 minutes, possibly due to clogging in part of the aperture. The control experiment also shows a slight decrease in permeability, possibly due to changes in the saturation level of the fracture. Although all samples were saturated with DI water until the pressure stabilized before injecting the solutions, a slight change was observed in the saturation when the inlet was unplugged to refill the syringes. As a result, the estimated permeability at the beginning of the precipitation experiment may not reflect the actual permeability. When calculating the fracture aperture reduction from the pressure difference using the cubic law (**Table 3**), the average differential pressure of the control experiment was taken as the initial reference value. This corresponded to a fracture aperture reduction of 43.98 µm and 44.19 µm for the 12H and 16H experiments, respectively.

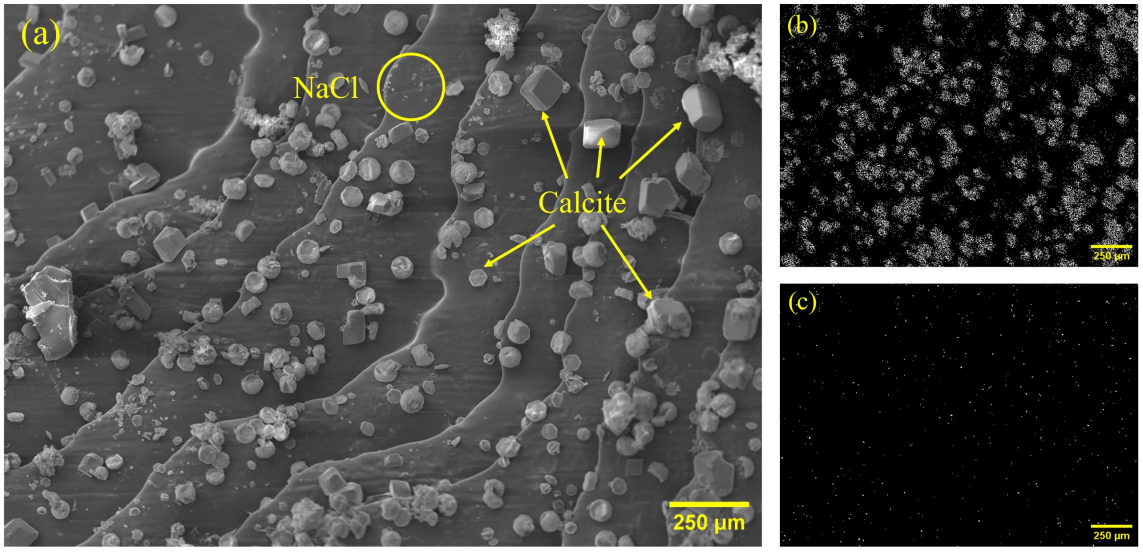

Figure 4: Secondary electron image of fracture surface after precipitation experiment showing **(a)** calcite and NaCl grains, and associated elemental maps of **(b)** calcium and **(c)** sodium.

 https://doi.org/10.69631/dpd8ha46

3.4. SEM-EDS Analysis

The high-resolution secondary electron SEM images and EDS elemental maps (**Fig. 5**) reveal the composition and morphology of the precipitates on the printed fractured surface. The corrugated texture of the printed material resulted from the layer-by-layer fabrication method inherent to the DLP printing technique. On the fracture surface, rhombohedral calcite crystals are mainly observed (**Fig. 5a**) as well as some rounded shapes. A small amount of sodium chloride salt is also detected on the surface, as confirmed by the elemental map of sodium (**Fig. 5c**).

4. DISCUSSION

The contact angle of the printed polymer sample provides insight into its wettability, water affinity, and surface energy. The average measured contact angle for DI water on the printed films is 49.83° (**Fig. 1b**), indicating decent wettability and moderate surface energy, as the contact angle is inversely related to the surface energy (59). As surface roughness is known to influence contact angles (27, 55), and since increased surface roughness in hydrophilic materials tends to reduce the contact angle (1), the wettability of the printed fracture sample is therefore expected to be higher. This condition is quite favorable for adhesion and crystal formation as the surface is neither too repellent nor too absorbent. Comparing this to natural samples, shale wettability has a wide range reported in the literature depending on the composition (47) and surface roughness (28). While Borysenko et al. (5) reported air–water contact angles for hydrophilic shale as low as 10°–30° and up to 120° for hydrophobic shale, depending on mineralogy (clay and quartz content), Mokhtari et al. (32) investigated the effect of total organic carbon (TOC) and observed air–water contact angles ranging from 8° to 101° for samples with varying TOC. Engelder et al. measured an air/water contact angle of 50.69° for Marcellus shale, which is rich in carbonate and has a high amount of TOC (12 wt%) (14).

Fourier transform infrared spectroscopy results confirm the presence of carbonyl and ester groups on the surface of the resin. These groups are known for their polarity, volatility, and reactivity due to the presence of oxygen with partial electronegativity (10). Carbon and oxygen's relative electronegativity, or ability to attract electrons, makes the carbonyl group polar and hence energizes the surface. This would be favorable to attract precipitating ions and initiate mineral formation.

Roughness and texture parameters provide key insights into the variation in surface pattern and asperities. The profile maps and the roughness parameters show similar results among the samples. The average surface roughness for the samples is 32.14 µm, and the standard deviation is 0.58. A considerably small standard deviation compared to the mean suggests a good replicability. Typical surface roughness of fractured rock ranges from microns (39) to a couple of millimeters (60). depending on the morphology of the sample. The average surface roughness of the 3D-printed fracture surfaces considered in this study is within the range of natural samples, suggesting the viability of such samples for reflecting real fractured samples.

The evolution of effluent ion concentration of calcium indicates calcite precipitation during the flow-through fracture experiments and changes in differential pressure suggest a decline in permeability. The difference between fracture aperture reduction estimated from effluent concentration and 3D X-ray CT scans suggests the potential for unaccounted calcite precipitation occurring outside the fracture. However, a comparatively higher reduction is estimated from the cubic law. This is because the cubic law estimates hydraulic aperture, whereas 3D X-ray imaging yields the physical or geometric aperture. As hydraulic aperture is based on fluid flow resistance, it is inherently more sensitive to localized constriction due to heterogeneous precipitation. Moreover, the cubic law assumes a parallel plate without considering any roughness on the surface and assumes that the flow through the fracture is laminar without any turbulence. However, real fractures have uneven aperture and highly rough surfaces; this results in deviation in flow pattern and if the flow becomes turbulent locally, the relationship between pressure drop and flow rate is no longer linear (26).

The X-ray CT images of the reacted samples facilitate analysis of the regions where precipitation has occurred most. In both samples, the precipitate is more significant near the inlet where the freshly mixed solution enters, and the saturation levels are highest. Noiriel et al. observed similar results and reported the dependency of local saturation index on calcite precipitation (35). A high saturation index and far from equilibrium condition near the inlet results in rapid precipitation in that region. Moreover, some localized calcite precipitation is observed in regions where the aperture size transitions sharply from large to small. Studies have shown that heterogenous nucleation is more likely to occur on surface irregularities like steps, edges, tips or constrictions (40). This is because elevated local curvature reduces critical supersaturation for nucleation (49) and high surface energy at irregularities promotes growth to minimize overall energy (33). Moreover, constricted flow path elevates local saturation (29) resulting in more precipitation.

The permeability evolution over time shows a decreasing trend. Trendlines are derived from the permeability data. Measurements of the initial two hours are skipped as steady state conditions may not have been achieved at the beginning. This results in a similar exponential equation and R^2 value of ~0.95 for both experiments. Each equation has a negative exponential coefficient, meaning a decaying function, and the smaller magnitude (-0.005 and -0.006) indicates a very slow decay. That means the rate of permeability reduction due to precipitation decreases over time. As precipitation occurs, it reduces the fracture aperture, resulting in an increase in overall flow velocity. A higher velocity means shorter residence time, which may limit the chance for precipitation to occur because the dissolved ions are quickly swept away before they can accumulate to form solids. As a result, the process slows down the overall fracture-sealing mechanism.

The SEM-SE and EDS analysis confirms the precipitation of calcite and provides critical morphological information of the crystals. The heterogeneous nucleation results in anisotropic growth, causing crystals to form in both subhedral and euhedral shapes. Subhedral crystal occurs due to various reasons such as variation in saturation, rapid growth rates, impurities in the solution etc. (17) that result in partial development of well-defined crystal faces. On the other hand, a very small amount of sodium chloride was observed, which may have formed during the drying phase as it precipitated from the residual solution remaining within the fracture.

5. CONCLUSION

This study presented the use of fabricated fractured samples to study the evolution of fracture aperture and permeability evolution. Contact angle measurement and FTIR spectroscopy showed the suitability of the material for promoting calcite precipitation. Furthermore, characterization of the fracture surface using light interferometry on three different samples yielded similar results, demonstrating the high repeatability of the sample fabrication process.

Pore pressure, effluent ion concentrations, and time lapsed X-ray micro-CT imaging show a decrease in fracture permeability due to carbonate mineralization. The average theoretical aperture reduction estimated from the 3D X-ray CT image was slightly higher than the estimation from the effluent ion concentration. This slight difference might come from the unaccounted precipitation occurring outside of the fracture in the tubing. In contrast, the calculated fracture aperture reduction derived from the cubic law was considerably higher than the measurements from the other approaches, as it determines the hydraulic aperture versus the mechanical aperture from 3D X-ray imaging. Moreover, the cubic law's assumption of a parallel flat surface oversimplifies the actual fracture geometry, resulting in a higher estimated aperture reduction.

The 3D X-ray CT image of the precipitation shows some zonal preferences, affected mainly by the sudden changes in the local velocity due to fracture aperture change. The study demonstrated replicable experiments revealing consistent precipitation patterns in relation to fracture geometry. This confirms the significant role of the fracture geometry in determining where the precipitation occurs. The study also showed a relation between calcite precipitation and permeability change. Additionally, the work introduced a novel technique for the first time that enables an improved understanding of carbonate

mineralization in fractured systems, effectively overcoming the challenges associated with using natural samples. Calcite precipitation occurs naturally in carbonate karst or in fractured reservoirs due to anthropogenic CO_2 injections. Understanding fracture aperture evolution due to calcite precipitation will aid in groundwater quality management and remediation design, as well as in predicting fracture sealing for assessing the long-term stability of CO_2 storage sites. It will also pave the way for applying the same model in both simulations and experiments, allowing experimental results to be directly used for calibrating or benchmarking numerical models in PFLOTRAN, TOUGHREACT, OpenFOAM, and similar platforms.

STATEMENTS AND DECLARATIONS

Supplementary Material

The following supporting information is available online with this article: detailed methodology for calculating the surface roughness parameter, a schematic of the experimental setup, and SEM images of 2D films showing calcite precipitation.

Acknowledgements

This project is supported by the Southeast Regional CO_2 Utilization and Storage Partnership (SECARB-USA), funded by the U.S. Department of Energy and cost-sharing partners under grant number FE0031830, managed by the Southern States Energy Board. Thin film experiments supported by the National Science Foundation under grant No. 2025626.

Author Contributions

Md Fahim Salek: Conceptualization, Formal analysis, Investigation, Methodology, Visualization, Writing – original draft. Harrish Kumar Senthil Kumar: Investigation, Methodology. Abdullah Al Nahian: Investigation, Methodology. Samsul Mahmood: Formal analysis, Methodology. Bryan S. Beckingham: Supervision. Kyle Schulze: Supervision. Lauren E. Beckingham: Funding acquisition, Supervision, Writing – review & editing.

Conflicts of Interest

The authors declare no conflict of interest.

Data, Code & Protocol Availability

The data underlying this study are openly available in Zenodo at: https://doi.org/10.5281/zenodo.14625465.

Funding Received

Funding for this study was received from the Office of Fossil Energy and Carbon Management (FE0031830), https://doi.org/10.13039/100020312), Division of Earth Sciences (2025626), https://doi.org/10.13039/100000160).

ORCID IDs

Md Fahim Salek https://orcid.org/0009-0000-1801-525X
Harrish Kumar Senthil Kumar https://orcid.org/0009-0003-4312-808X
Abdullah Al Nahian https://orcid.org/0000-0001-8368-8178
Samsul Mahmood https://orcid.org/0000-0003-3595-3891
Bryan S. Beckingham https://orcid.org/0000-0003-4004-0755
Kyle Schulze https://orcid.org/0000-0001-8433-0581
Lauren E. Beckingham https://orcid.org/0000-0002-8433-9532

REFERENCES

1. Ahmad, D., Van Den Boogaert, I., Miller, J., Presswell, R., & Jouhara, H. (2018). Hydrophilic and hydrophobic materials and their applications. *Energy Sources, Part A: Recovery, Utilization, and Environmental Effects*, 40(22), 2686–2725. https://doi.org/10.1080/15567036.2018.1511642
2. Anjikar, I. S., Wales, S., & Beckingham, L. E. (2020). Fused Filament Fabrication 3-D Printing of Reactive Porous Media. *Geophysical Research Letters*, 47(9), 1–9. https://doi.org/10.1029/2020GL087665
3. Bashir, A., Ali, M., Patil, S., Aljawad, M. S., Mahmoud, M., et al. (2024). Comprehensive review of CO_2 geological storage: Exploring principles, mechanisms, and prospects. *Earth-Science Reviews*, 104672. https://doi.org/10.1016/j.earscirev.2023.104672
4. Borrok, D. M., Yang, W., Wei, M., & Mokhtari, M. (2019). Heterogeneity of the mineralogy and organic content of the Tuscaloosa Marine Shale. *Marine and Petroleum Geology*, 109, 717–731. https://doi.org/10.1016/j.marpetgeo.2019.06.056
5. Borysenko, A., Clennell, B., Sedev, R., Burgar, I., Ralston, J., et al. (2009). Experimental investigations of the wettability of clays and shales. *Journal of Geophysical Research: Solid Earth*, 114(B7). https://doi.org/10.1029/2008JB005928
6. Brunet, J.-P. L., Li, L., Karpyn, Z. T., & Huerta, N. J. (2016). Fracture opening or self-sealing: Critical residence time as a unifying parameter for cement–CO_2–brine interactions. *International Journal of Greenhouse Gas Control*, 47, 25–37. https://doi.org/10.1016/j.ijggc.2016.01.024
7. Cao, P., Karpyn, Z. T., & Li, L. (2015). Self-healing of cement fractures under dynamic flow of CO_2-rich brine. *Water Resources Research*, 51(6), 4684–4701. https://doi.org/10.1002/2014WR016162
8. Carroll, S., Carey, J. W., Dzombak, D., Huerta, N. J., Li, L., et al. (2016). Role of chemistry, mechanics, and transport on well integrity in CO_2 storage environments. *International Journal of Greenhouse Gas Control*, 49, 149–160. https://doi.org/10.1016/j.ijggc.2016.01.010
9. Caulk, Robert A., Ehsan Ghazanfari, Julia N. Perdrial, and Nico Perdrial. Experimental investigation of fracture aperture and permeability change within Enhanced Geothermal Systems. *Geothermics* 62 (2016): 12-21. https://doi.org/10.1016/j.geothermics.2016.02.003
10. Costa, P., Pilli, R., Pinheiro, S., & Bakuzis, P. (2022). The Chemistry of Carbonyl Compounds and Derivatives. Royal Society of Chemistry. https://doi.org/10.1039/9781837670888
11. De Yoreo, J. J., Gilbert, P. U. P. A., Sommerdijk, N. A. J. M., Penn, R. L., Whitelam, S., et al. (2015). Crystallization by particle attachment in synthetic, biogenic, and geologic environments. *Science*, 349(6247), aaa6760. https://doi:10.1126/science.aaa6760
12. De Yoreo, J. J., & Vekilov, P. G. (2003). Principles of crystal nucleation and growth. *Reviews in Mineralogy and Geochemistry*, 54(1), 57–93. https://doi.org/10.2113/0540057
13. Dilsiz, E. A., & Mihcakan, I. M. (2023). The effects of calcium carbonate precipitation on high-velocity flow behavior in 3D printed fracture models. *Geoenergy Science and Engineering*, 221, 111264. https://doi.org/10.1016/j.petrol.2022.111264
14. Engelder, T., Cathles, L. M., & Bryndzia, L. T. (2014). The fate of residual treatment water in gas shale. *Journal of Unconventional Oil and Gas Resources*, 7, 33–48. https://doi.org/10.1016/j.juogr.2014.03.002
15. Fatah, A., Bennour, Z., Ben Mahmud, H., Gholami, R., & Hossain, M. M. (2020). A review on the influence of CO2/shale interaction on shale properties: Implications of CCS in shales. *Energies*, 13(12), 3200. https://doi.org/10.3390/en13123200
16. Fatah, A., Mahmud, H. Ben, Bennour, Z., Gholami, R., & Hossain, M. (2022). Geochemical modelling of CO2 interactions with shale: Kinetics of mineral dissolution and precipitation on geological time scales. *Chemical Geology*, 592, 120742. https://doi.org/10.1016/j.chemgeo.2022.120742
17. Folk, R. L. (1979). The Natural History of Crystalline Calcium Carbonate: Effect of Magnesium Content and Salinity[1]. https://doi.org/10.1306/CE11401C6
18. Griffiths, L., Heap, M. J., Wang, F., Daval, D., Gilg, H. A., et al. (2016). Geothermal implications for fracture-filling hydrothermal precipitation. *Geothermics*, 64, 235–245. https://doi.org/10.1016/j.geothermics.2016.06.006
19. Huang, H., & Dong, M. (2024). CO_2 containment and storage in organic-rich strata–State of the art and future directions. *International Journal of Greenhouse Gas Control*, 132, 104047. https://doi.org/10.1016/j.ijggc.2023.104047
20. Ishutov, S., & Hasiuk, F. J. (2017). 3D printing Berea sandstone: testing a new tool for petrophysical analysis of reservoirs. *Petrophysics*, 58(06), 592–602.

https://www.researchgate.net/publication/320863880_3D_Printing_Berea_Sandstone_Testing_a_New_Tool_for_Petrophysical_Analysis_of_Reservoirs

21. Jia, Y., Lu, Y., Tang, J., Fang, Y., Xia, B., & Ge, Z. (2018). Mechanical-chemical-mineralogical controls on permeability evolution of shale fractures. *Geofluids*, 2018(1), 7801843. https://doi.org/10.1155/2018/7801843
22. Kong, L., Ishutov, S., Hasiuk, F., & Xu, C. (2021). 3D printing for experiments in petrophysics, rock physics, and rock mechanics: a review. *SPE Reservoir Evaluation & Engineering*, 24(04), 721–732. https://doi.org/10.2118/206744-PA
23. Kumar, H. K. S., Al Nahian, A., Braziel, N., Shi, Z., Torrance, M., et al. (2025). 3D Printing Reactive Porous Media: Calcite Precipitation Kinetics on Surface Functionalized Polymer Films and 3D-printed Cores. *InterPore Journal*, 2(2), IPJ040625-7. https://doi.org/10.69631/ipj.v2i2nr71
24. Lasaga, A. C. (1984). Chemical kinetics of water-rock interactions. *Journal of Geophysical Research: Solid Earth*, 89(B6), 4009–4025. https://doi.org/10.1029/JB089iB06p04009
25. Li, B., Wang, J., Liu, R., & Jiang, Y. (2021a). Nonlinear fluid flow through three-dimensional rough fracture networks: Insights from 3D-printing, CT-scanning, and high-resolution numerical simulations. *Journal of Rock Mechanics and Geotechnical Engineering*, 13(5), 1020–1032. https://doi.org/10.1016/j.jrmge.2021.04.007
26. Li, B., Wang, J., Liu, R., & Jiang, Y. (2021b). Nonlinear fluid flow through three-dimensional rough fracture networks: Insights from 3D-printing, CT-scanning, and high-resolution numerical simulations. *Journal of Rock Mechanics and Geotechnical Engineering*, 13(5), 1020–1032. https://doi.org/10.1016/j.jrmge.2021.04.007
27. Li, C., Zhang, J., Han, J., & Yao, B. (2021). A numerical solution to the effects of surface roughness on water–coal contact angle. *Scientific Reports*, 11(1), 459. https://doi:10.1038/s41598-020-80729-9
28. Li, P., Zhang, J., Rezaee, R., Dang, W., Li, X., et al. (2021). Effects of swelling-clay and surface roughness on the wettability of transitional shale. *Journal of Petroleum Science and Engineering*, 196, 108007. https://doi.org/10.1016/j.petrol.2020.108007
29. Mahmoudzadeh, B., Liu, L., Moreno, L., & Neretnieks, I. (2013). Solute transport in fractured rocks with stagnant water zone and rock matrix composed of different geological layers—Model development and simulations. *Water Resources Research*, 49(3), 1709–1727. https://doi.org/10.1002/wrcr.20132
30. Major, J. R., Eichhubl, P., Dewers, T. A., & Olson, J. E. (2018). Effect of CO_2–brine–rock interaction on fracture mechanical properties of CO_2 reservoirs and seals. *Earth and Planetary Science Letters*, 499, 37–47. https://doi.org/10.1016/j.epsl.2018.07.013
31. Martinez, M. J., Yoon, H., Kucala, A., Dewers, T., & Mendoza, H. (2017). Digital rock physics and 3D printing for fractured porous media. Sandia National Lab.(SNL-NM), Albuquerque, NM (United States). https://doi.org/10.2172/1603850
32. Mokhtari, M., Alqahtani, A. A., Tutuncu, A. N., & Yin, X. (2013). Stress-dependent permeability anisotropy and wettability of shale resources. SPE/AAPG/SEG Unconventional Resources Technology Conference, URTEC-1555068. https://doi.org/10.1190/urtec2013-283
33. Nancollas, G. H. (1979). The growth of crystals in solution. Advances in Colloid and Interface Science, 10(1), 215–252. https://doi.org/10.1016/0001-8686(79)87007-4
34. Nilsson, Ö., & Sternbeck, J. (1999). A mechanistic model for calcite crystal growth using surface speciation. *Geochimica et Cosmochimica Acta*, 63(2), 217–225. https://doi.org/10.1016/S0016-7037(99)00026-5
35. Noiriel, C., Seigneur, N., Le Guern, P., & Lagneau, V. (2021). Geometry and mineral heterogeneity controls on precipitation in fractures: An X-ray micro-tomography and reactive transport modeling study. *Advances in Water Resources*, 152, 103916. https://doi.org/10.1016/j.advwatres.2021.103916
36. Patiño, J. E., Miele, F., Perez, A. J., Kanavas, Z., Dughi, M. L., & Morales, V. L. (2024). Replication of soil analogues at the original scale by 3D printing: Quantitative assessment of accuracy and repeatability of the pore structural heterogeneity. *Advances in Water Resources*, 104795. https://doi.org/10.1016/j.advwatres.2024.104795
37. Phillips, T., Bultreys, T., Bisdom, K., Kampman, N., Van Offenwert, S., et al. (2021). A systematic investigation into the control of roughness on the flow properties of 3D-printed fractures. *Water Resources Research*, 57(4), ewrcr-25233. https://doi.org/10.1029/2020WR028671
38. Phillips, T., Inskip, N. D. F., Esegbue, O., Borisochev, G., Bultreys, T., et al. (2020). Laboratory-based investigation into the fluid flow properties of natural and 3D-printed rough fractures. 1st Geoscience & Engineering in Energy Transition Conference, 2020(1), 1–5. https://doi.org/10.3997/2214-4609.202021014
39. Qu, G., Shi, T., Zhang, Z., Su, J., Wei, H.,et al. (2022). Characteristics description of shale fracture surface morphology: A case study of shale samples from Barnett Shale. *Processes*, 10(2), 401. https://doi.org/10.3390/pr10020401

40. Rodrigues, N. T., Carrasco, I. S. S., Voller, V. R., & Aarão Reis, F. D. A. (2024). Mineral Deposition on the Rough Walls of a Fracture. *Minerals*, 14(12), 1213. https://doi.org/10.3390/min14121213
41. Salek, M. F., Shinde, V. V., Beckingham, B. S., & Beckingham, L. E. (2022). Resin based 3D printing for fabricating reactive porous media. *Materials Letters*, 322. https://doi.org/10.1016/j.matlet.2022.132469
42. Sander, R., Pan, Z., & Connell, L. D. (2017). Laboratory measurement of low permeability unconventional gas reservoir rocks: A review of experimental methods. *Journal of Natural Gas Science and Engineering*, 37, 248–279. https://doi.org/10.1016/j.jngse.2016.11.041
43. Schindelin, J., Arganda-Carreras, I., Frise, E., Kaynig, V., Longair, M., et al. (2012). Fiji: an open-source platform for biological-image analysis. *Nature Methods*, 9(7), 676–682.
44. Schultz, L. G. (1964). Quantitative interpretation of mineralogical composition from X-ray and chemical data for the Pierre Shale. https://doi.org/10.3133/pp391C
45. Sharifigaliuk, H., Mahmood, S. M., Rezaee, R., & Saeedi, A. (2021). Conventional methods for wettability determination of shales: A comprehensive review of challenges, lessons learned, and way forward. *Marine and Petroleum Geology*, 133, 105288. https://doi.org/10.1016/j.marpetgeo.2021.105288
46. Shinde, V. V, Wang, Y., Salek, M. F., Auad, M. L., Beckingham, L. E., & Beckingham, B. S. (2022). Material design for enhancing properties of 3D printed polymer composites for target applications. *Technologies*, 10(2), 45. https://doi.org/10.3390/technologies10020045
47. Siddiqui, M. A. Q., Ali, S., Fei, H., & Roshan, H. (2018). Current understanding of shale wettability: A review on contact angle measurements. *Earth-Science Reviews*, 181, 1–11. https://doi.org/10.1016/j.earscirev.2018.04.002
48. Song, C., Elsworth, D., Jia, Y., & Lin, J. (2022). Permeable rock matrix sealed with microbially-induced calcium carbonate precipitation: Evolutions of mechanical behaviors and associated microstructure. *Engineering Geology*, 304, 106697. https://doi.org/10.1016/j.enggeo.2022.106697
49. Stack, A. G. (2015). Precipitation in pores: A geochemical frontier. *Reviews in Mineralogy and Geochemistry*, 80(1), 165–190. https://doi.org/10.2138/rmg.2015.80.05
50. Starchenko, V. (2022). Pore-scale modeling of mineral growth and nucleation in reactive flow. *Frontiers in Water*, 3, 800944. https://doi.org/10.3389/frwa.2021.800944
51. Stoner, D. L., Watson, S. M., Stedtfeld, R. D., Meakin, P., Griffel, L. K., et al. (2005). Application of stereolithographic custom models for studying the impact of biofilms and mineral precipitation on fluid flow. *Applied and Environmental Microbiology*, 71(12), 8721–8728. https://doi.org/10.1128/AEM.71.12.8721-8728.2005
52. Suzuki, A., Minto, J. M., Watanabe, N., Li, K., & Horne, R. N. (2019). Contributions of 3D printed fracture networks to development of flow and transport models. *Transport in Porous Media*, 129, 485–500. https://doi.org/10.1007/s11242-018-1154-7
53. Tartakovsky, A. M., Meakin, P., Scheibe, T. D., & Wood, B. D. (2007). A smoothed particle hydrodynamics model for reactive transport and mineral precipitation in porous and fractured porous media. *Water Resources Research*, 43(5). https://doi.org/10.1029/2005WR004770
54. Wagner, R., Kühn, M., Meyn, V., Pape, H., Vath, U., & Clauser, C. (2005). Numerical simulation of pore space clogging in geothermal reservoirs by precipitation of anhydrite. *International Journal of Rock Mechanics and Mining Sciences*, 42(7–8), 1070–1081. https://doi.org/10.1016/j.ijrmms.2005.05.008
55. Wang, J., Wu, Y., Cao, Y., Li, G., & Liao, Y. (2020). Influence of surface roughness on contact angle hysteresis and spreading work. *Colloid and Polymer Science*, 298, 1107–1112. https://doi:10.1007/s00396-020-04680-x
56. Wang, L., Cardenas, M. B., Zhou, J., & Ketcham, R. A. (2020). The complexity of nonlinear flow and non-Fickian transport in fractures driven by three-dimensional recirculation zones. *Journal of Geophysical Research: Solid Earth*, 125(9), e2020JB020028. https://doi.org/10.1029/2020JB020028
57. Witherspoon, P. A., Wang, J. S. Y., Iwai, K., & Gale, J. E. (1980). Validity of cubic law for fluid flow in a deformable rock fracture. *Water Resources Research*, 16(6), 1016–1024. https://doi.org/10.1029/WR016i006p01016
58. Yang, F., Stack, A. G., & Starchenko, V. (2021). Micro-continuum approach for mineral precipitation. *Scientific Reports*, 11(1), 3495. https://doi.org/10.1038/s41598-021-82807-y
59. Yang, J.-T., Yang, Z.-H., Chen, C.-Y., & Yao, D.-J. (2008). Conversion of surface energy and manipulation of a single droplet across micropatterned surfaces. *Langmuir*, 24(17), 9889–9897. https://doi.org/10.1021/la8004695

60. Zhang, C. P., Cheng, P., Ranjith, P. G., Lu, Y. Y., & Zhou, J. P. (2020). A comparative study of fracture surface roughness and flow characteristics between CO_2 and water fracturing. *Journal of Natural Gas Science and Engineering*, 76, 103188. https://doi.org/10.1016/j.jngse.2020.103188